minerals

MDPI

Article

Formation of Spessartine and CO_2 via Rhodochrosite Decarbonation along a Hot Subduction P-T Path

Yuliya V. Bataleva [1,*], Aleksei N. Kruk [1], Ivan D. Novoselov [1,2] and Yuri N. Palyanov [1,2,*]

1 Sobolev Institute of Geology and Mineralogy, Siberian Branch of Russian Academy of Sciences, 630090 Novosibirsk, Russia; krukan@igm.nsc.ru (A.N.K.); novoselovid@igm.nsc.ru (I.D.N.)
2 Department of Geology and Geophysics, Novosibirsk State University, 630090 Novosibirsk, Russia
* Correspondence: bataleva@igm.nsc.ru (Y.V.B.); palyanov@igm.nsc.ru (Y.N.P.); Tel.: +7-383-330-75-01 (Y.N.P.)

Received: 13 July 2020; Accepted: 5 August 2020; Published: 7 August 2020

Abstract: Experimental simulation of rhodochrosite-involving decarbonation reactions resulting in the formation of spessartine and CO_2-fluid was performed in a wide range of pressures (*P*) and temperatures (*T*) corresponding to a hot subduction *P-T* path. Experiments were carried out using a multi-anvil high-pressure apparatus of a "split-sphere" type (BARS) in an $MnCO_3$–SiO_2–Al_2O_3 system (3.0–7.5 GPa, 850–1250 °C and 40–100 h.) with a specially designed high-pressure hematite buffered cell. It was experimentally demonstrated that decarbonation in the $MnCO_3$–SiO_2–Al_2O_3 system occurred at 870 ± 20 °C (3.0 GPa), 1070 ± 20 °C (6.3 GPa), and 1170 ± 20 °C (7.5 GPa). Main Raman spectroscopic modes of the synthesized spessartine were 349–350 (R), 552(v_2), and 906–907 (v_1) cm^{-1}. As evidenced by mass spectrometry (IRMS) analysis, the fluid composition corresponded to pure CO_2. It has been experimentally shown that rhodochrosite consumption to form spessartine + CO_2 can occur at conditions close to those of a hot subduction *P-T* path but are 300–350 °C lower than pyrope + CO_2 formation parameters at constant pressures. We suppose that the presence of rhodocrosite in the subducting slab, even as solid solution with Mg,Ca-carbonates, would result in a decrease of the decarbonation temperatures. Rhodochrosite decarbonation is an important reaction to explain the relationship between Mn-rich garnets and diamonds with subduction/crustal isotopic signature.

Keywords: spessartine; CO_2 fluid; rhodochrosite; manganese; decarbonation; subduction; mantle; high-pressure experiment

1. Introduction

Manganese is a 3*d* transition metal that can have various valences (1, 2, 3, 4, 6, 7) and spin states; this element is one of the most common in the Earth's crust and mantle (12th and 11th in terms of abundance) and in the bulk Earth (12th in terms of abundance [1–4]). The greatest amount of Mn is contained in the oceanic crust in ferromanganese nodules as oxides and in marine sediments as Mn-carbonate (rhodochrosite) [5]. As shown in a number of modern experimental works on the behavior of rhodochrosite and Mn-oxides at high temperatures and pressures, these minerals can be thermodynamically stable to ultrahigh pressure (*P*) and temperature (*T*) conditions (Figure 1) [6–12]. However, during subduction of the oceanic crust, Mn-rich oxides and rhodochrosite not only are transported to the mantle but interact with mantle rocks, leaving characteristic chemical "traces" in mantle rocks, most pronounced in garnet-bearing assemblages. These "traces" consist of a sharp increase in the concentrations of the spessartine component (as well as almandine) in garnets, the presence of carbon phases (diamond, graphite, C-O-H fluid), as well as the "subduction carbon isotopic signature" or "crustal oxygen isotopic signature" [13–17]. Similar "traces" are also described in diamond-bearing rocks of ultra-high pressure (UHP) terranes [18–20].

Analysis of modern data shows evidence for a direct relationship between Mn-rich minerals and diamond. There are four described large occurrences: (1) diamonds of eclogite paragenesis with inclusions of Fe,Mn-rich garnet from the Finsch kimberlite pipe, South Africa [13–15]; (2) microdiamond inclusions in Mn-rich garnet from Western Alps UHP terrain [18,19] and (3) Kokchetav massif, Kazakhstan [21]; (4) diamond with Mn-rich ilmenite inclusions from kimberlitic rocks of Juina, Brazil [22]. A potential genetic relationship of diamond and rhodochrosite was experimentally demonstrated by Liu et al. [7]. They have shown that rhodochrosite can dissociate into Mn_3O_4 + graphite + O_2 (P = 60–80 kbar; T > 2000 °C) and Mn_3O_4 + diamond + O_2 (P > 120 kbar; T > 2000 °C).

The interconnection between rhodochrosite, spessartine, and carbon-bearing phases under subduction settings can be described in terms of the following decarbonation reactions:

$$3MnCO_3 + 3SiO_2 + Al_2O_3 \rightarrow Mn_3Al_2Si_3O_{12} + 3CO_2 \quad (1)$$

$$3MnCO_3 + Al_2SiO_5 + 2SiO_2 \rightarrow Mn_3Al_2Si_3O_{12} + 3CO_2 \quad (2)$$

However, there is a lack of experimental studies of rhodochrosite-involving decarbonation reactions. Previously, decarbonation reactions resulting in the formation of pyrope (or pyrope-almandine) were experimentally studied by [23–25], and theoretical positions of some decarbonation reactions were calculated by [26,27]. The main goal of this study is to experimentally simulate the rhodochrosite-involving decarbonation reactions, resulting in the formation of spessartine and CO_2-fluid, in a wide range of pressures and temperatures, with implications to the Mn-carbonate stability and spessartine formation under hot subduction conditions.

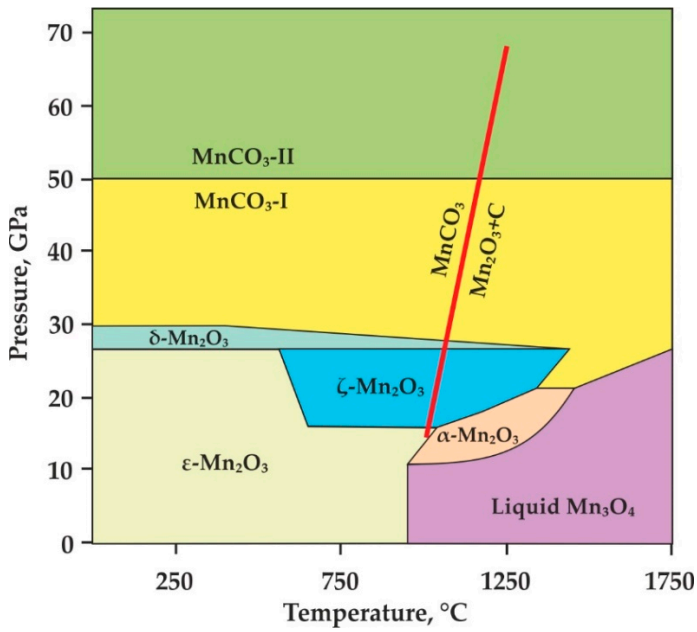

Figure 1. Pressure (P)-temperature (T) diagram for $MnCO_3$ and Mn_2O_3 stability after [12,28]. $MnCO_3$-I-rhombohedral structure (rhodochrosite), $MnCO_3$-II-triclinic structure high-pressure polymorph.

2. Materials and Methods

2.1. High-Pressure High-Temperature Experimental Methods

Experimental simulation of decarbonation reactions in the system $MnCO_3$-SiO_2-Al_2O_3 was carried out using a multi-anvil high-pressure split-sphere apparatus (BARS) [29,30] at pressures of 3.0, 6.3, and 7.5 GPa, in the temperature range of 850–1250 °C and durations from 40 to 100 h. Natural rhodochrosite $Mn_{0.97}Fe_{0.02}Mg_{0.01}Ca_{0.01}CO_3$ (China, Guangxi Zhuang Autonomous Region, Wuzhou Prefecture, Cangwu Co., Wutong Mine (Wudong Mine)) (Figure 2) as well as synthetic oxides SiO_2

and Al_2O_3 (99.99% purity) were used as starting reagents. Before the experiments, the reagents were powdered and thoroughly mixed. The weight proportions of the starting $MnCO_3$, SiO_2, and Al_2O_3 were 55:29:16 (wt.%); they were selected stoichiometrically according to the decarbonation reaction (1). Weights of $MnCO_3$, SiO_2, and Al_2O_3 depended on capsule sizes and corresponded to 5.5, 2.9, and 1.6 mg (3.0 and 6.3 GPa) and 4.4, 2.3, and 1.3 mg (7.5 GPa). Methodological features of the assembly, the design of the high-pressure cell, as well as calibration data were published previously [31–33]. Based on previous experimental studies dealing with carbonate-oxide media [24] coupled with the generation of fluid in the initial solid-phase matrix as well as on recent data on the chemical reactivity between carbon dioxide and three transition metals [34], platinum was chosen as the material of the capsules. The volume of reaction capsules was selected to ensure that all necessary analytical methods could be employed, taking into account the size of the high pressure cell. The internal size of the Pt capsules for experiments at 3.0 and 6.3 GPa was 1.5 mm (diameter) with a length of 6 mm, and at 7.5 GPa, it was 1.5 mm with a length of 4 mm.

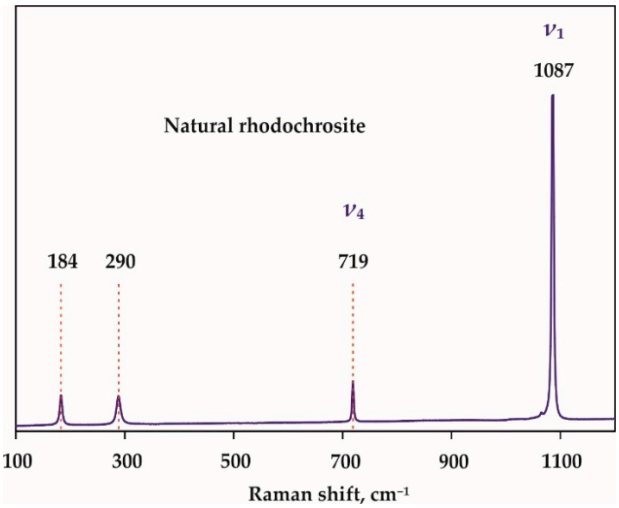

Figure 2. Raman spectrum of natural rhodochrosite $Mn_{0.97}Fe_{0.02}Mg_{0.01}Ca_{0.01}CO_3$ (China, Guangxi Zhuang Autonomous Region, Wuzhou Prefecture, Cangwu Co., Wutong Mine (Wudong Mine)). υ_1, υ_4—the high-frequency vibrational modes representing internal modes of the CO_3^{2-} group.

In high pressure (HP)-high temperature (HT) experiments, the problem of hydrogen diffusion through the capsules into the samples is well known [35,36]. This diffusion can result in a significant decrease in oxygen fugacity in the samples [35,36] and a corresponding temperature shift to the lower values of decarbonation curves. In this study, to prevent the influence of hydrogen influx on the course of the experiment, we used a specially designed high-pressure cell with a hematite container (buffer) [33]. The effective time of this buffer at temperatures <1200 °C was at least 150 h, and at 1500 °C, it was about 5 h. After the experiments, the chemical composition of the hematite buffer container was analyzed. In all cases, it was represented by hematite and magnetite (±wüstite), which indicates the effectiveness of the hematite buffer throughout the experiments. The duration of the experiments for each temperature was selected based on the effective time of the hematite buffer.

2.2. Analytical Methods

All analytical methods were performed in the Sobolev Institute of Geology and Mineralogy SB RAS and at the Analytical Center for multi-elemental and isotope research SB RAS. The samples obtained after the experiments were impregnated with epoxy resin, cut, and polished. The phase and the chemical compositions of the samples as well as the phase relationships were studied by electron scanning microscopy (SEM) and energy dispersive spectroscopy (EDS) (Tescan MIRA3 LMU scanning electron microscope, TESCAN, Brno, Czech Republic). Silicate phases were measured at an accelerating voltage of 20 kV, a probe current of 20 nA, a counting time of 10 s on each analytical line, and probe

diameter of 2–3 μm. The structural features of the obtained garnet crystals were studied by Raman spectroscopy (Jobin Yvon LabRAM HR800 spectrometer equipped with an Olympus BX41 stereo microscope, Horiba Jobin Yvon S.A.S., Lonjumeau, France). An He-Cd laser with a wavelength of 325 nm (Laser Quantum, Stockport, UK) was used as the excitation source. To control the effectiveness of the hematite buffer, the composition of the fluid phase was qualitatively determined by mass spectrometry. For this, the platinum ampoule after the experiment was placed in a vacuum device connected to a sample injection system in a Delta V Advantage Isotope Ratio Mass Spectrometer (IRMS) (Thermo Fisher Scientific, Bremen, Germany) and equipped with a special mechanism for piercing samples [37,38]. After preliminary evacuation of the device with the sample to a pressure of 2.7×10^{-2} mbar, guaranteeing the absence of atmospheric gases in the device, the ampoule was punctured, and the gas released at room temperature was let into the mass spectrometer analyzer.

3. Results

The parameters and the results of the experiments are presented in Table 1. Taking into account the previously developed approach and published results [23], the appearance of spessartine and CO_2 fluid in the reaction volume was considered as the main criterion for the decarbonation reaction.

Table 1. Experimental parameters and results of experiments in the $MnCO_3$-SiO_2-Al_2O_3 system.

Run N	*P*, GPa	*T*, °C	*t*, Hours	Final Mineral Phases
2131-R	3.0	850	100	Ky, Crn, Rds, Coe
2130-R	3.0	900	100	Sps, Ky, Crn, Rds
1744-R	3.0	950	60	Sps, Ky, Crn, Rds, Coe
1215-R	3.0	1000	60	Sps, Ky, Rds, Crn, Coe
2129-R	6.3	1050	60	Ky, Rds, Coe
2117-R	6.3	1100	40	Sps, Ky, Crn, Rds, Coe
2143-R	7.5	1150	60	Ky, Rds, Coe
2144-R	7.5	1200	60	Sps, Ky, Rds, Coe

Sps—spessartine, Rds—rhodochrosite, Coe—coesite, Crn—corundum, Ky—kyanite.

Accordingly, the formation of these phases was accompanied by a decrease in the amount of rhodochrosite. It must be emphasized that the partial conservation of carbonate and oxides in the samples is a consequence of the incomplete passage of the decarbonation reaction during the effective time of the hematite buffer.

Experimental studies in the $MnCO_3$-SiO_2-Al_2O_3 system were carried out in the temperature ranges 850–1000 °C (3.0 GPa), 1050–1100 °C (6.3 GPa), and 1150–1200 °C (7.5 GPa). At temperatures below the decarbonation reactions, the samples obtained were represented by recrystallized rhodochrosite and oxides as well as a small amount of newly formed kyanite (Figure 3a) at the corundum and the coesite contacts. At temperatures above the decarbonation reaction (Figure 3b–d), spessartine, kyanite, and recrystallized starting materials were formed in the samples. Fluid cavities were commonly observed in the matrix of the samples (e.g., Figure 3d). The composition of the obtained spessartine in all experiments corresponded to the formula $Mn_{2.84–2.96}Ca_{0.05}Fe_{0.05–0.09}Al_{1.94–2.05}Si_{2.95–3.02}O_{12}$ (Figure 4, Table 2). It was found that decarbonation in the $MnCO_3$-SiO_2-Al_2O_3 system occurred at 870 ± 20 °C (3.0 GPa), 1070 ± 20 °C (6.3 GPa), and 1170 ± 20 °C (7.5 GPa) (Figure 5a,b). As shown above, in the $MnCO_3$-SiO_2-Al_2O_3 system at temperatures exceeding the onset of decarbonation, the formation of fluid cavities was established in the samples (Figure 3d) formed as a result of the separation of the CO_2 fluid. The cavity size ranged from 10 to 200 μm. In a number of experiments, the composition of the fluid in the obtained samples was controlled by mass spectrometry. During the study, scanning the mass range from 12 to 46 amu revealed the presence of peaks at masses 44, 45, and 46, which corresponded exclusively to CO_2 (signals at other masses did not exceed background values). Thus, it was found that, in all samples, both in relatively low and high temperatures, the composition of the fluid corresponded to pure CO_2 without impurities of hydrogen or H_2O.

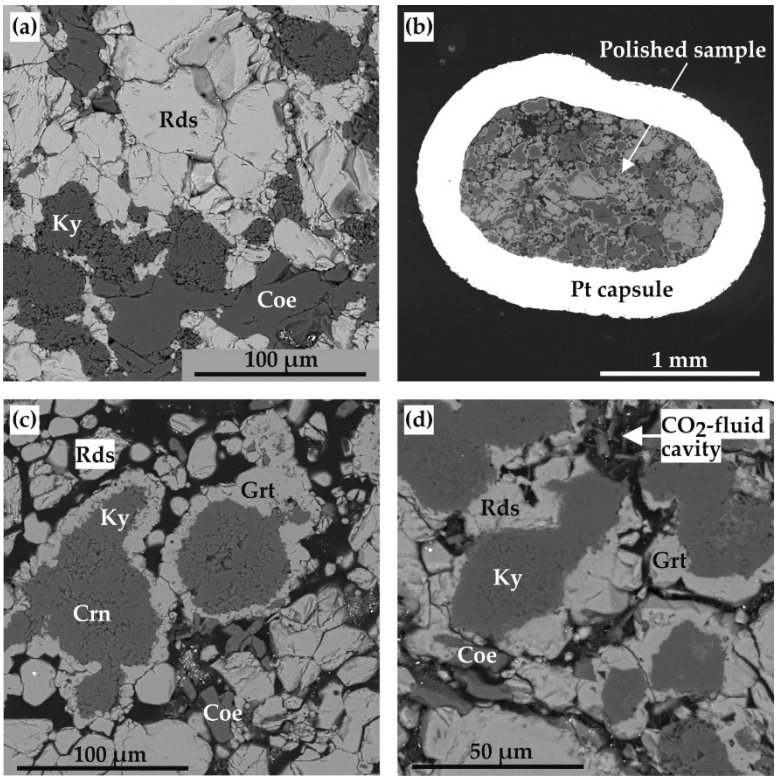

Figure 3. SEM micrographs of polished fragments of samples obtained in the $MnCO_3$-SiO_2-Al_2O_3 system: (**a**) polycrystalline aggregate of newly formed kyanite and recrystallized coesite and rhodochrosite (run N 2129-R, 6.3 GPa, 1050 °C); (**b**) a platinum ampoule with a sample (run N 2117-R, 6.3 GPa, 1100 °C); (**c**) polycrystalline aggregate of newly formed spessartine and kyanite and recrystallized initial oxides and rhodochrosite (run N 2117-R, 6.3 GPa, 1100 °C); (**d**) polycrystalline aggregate of spessartine, mullite, and recrystallized coesite, with CO_2-fluid cavities (run N 2130-R, 6.3 GPa, 1100 °C); Grt—spessartine garnet, Coe—coesite, Crn—corundum, Ky—kyanite, Rds—rhodochrosite.

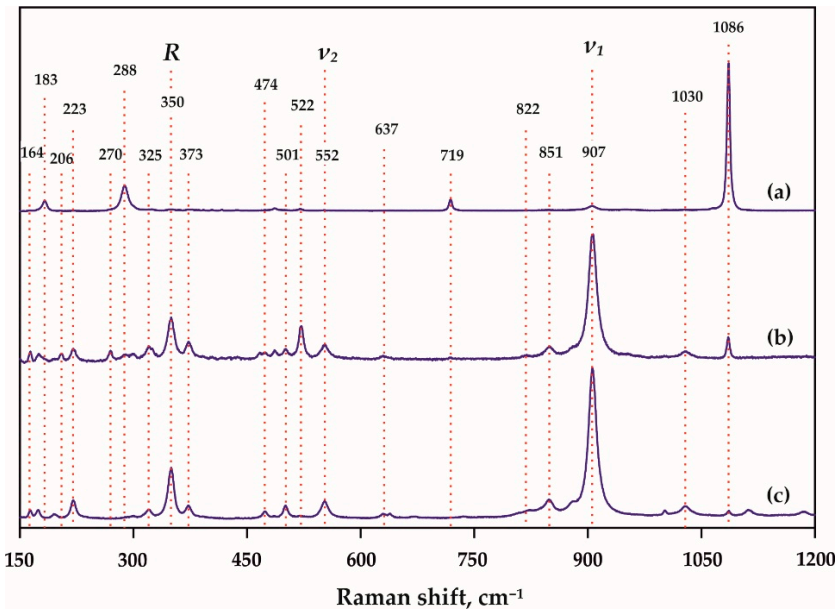

Figure 4. Representative Raman spectra of the obtained rhodochrosite ((**a**), run N 2129-R, 6.3 GPa, 1050 °C) and spessartine ((**b**) run N 1744-R, 3.0 GPa, 950 °C; (**c**) run N 2117-R, 6.3 GPa, 1100 °C). R, υ_1, υ_2—Modes, related to librational ($R(SiO_4)^{4-}$), internal bending ($(Si\text{-}O)_{bend}$, υ_2), and stretching ((Si-O)str, υ_1) vibrations of the SiO_4 tetrahedron, respectively.

Table 2. Averaged compositions of spessartine, kyanite, rhodochrosite, and oxides after experiments.

Run N	*P*, GPa	*T*, °C	Phase	Mass Concentrations, wt.%							n(O)	Cations Per Formula Unit						
				SiO_2	Al_2O_3	FeO	MnO	CaO	CO_2 *	Total		Si	Al	Fe	Mn	Ca	C *	Σ Cat
2131-R	3.0	850	Crn	-	$99.5_{(6)}$	-	$0.5_{(5)}$	-	-	100.0	3	-	$1.99_{(1)}$	-	$0.01_{(1)}$	-	-	2.00
			Rds	-	-	$2.0_{(4)}$	$58.0_{(6)}$	-	$40_{(1)}$	100.0	3	-	-	$0.03_{(1)}$	$0.92_{(2)}$	-	$1.02_{(1)}$	1.97
			Ky	$36.1_{(4)}$	$63.2_{(5)}$	-	$0.8_{(1)}$	-	-	100.1	5	$0.97_{(2)}$	$2.02_{(2)}$	-	$0.02_{(1)}$	-	-	3.01
			Coe	$99.9_{(1)}$	-	-	$0.1_{(1)}$	-	-	100.0	2	$1.00_{(1)}$	-	-	$0.01_{(1)}$	-	-	1.00
2130-R	3.0	900	Sps	$35.9_{(4)}$	$21.1_{(2)}$	$1.6_{(0)}$	$41.2_{(8)}$	$0.6_{(3)}$	-	100.5	12	$2.95_{(2)}$	$2.05_{(2)}$	$0.11_{(0)}$	$2.87_{(5)}$	$0.05_{(3)}$	-	8.03
			Crn	-	$99.3_{(8)}$	-	$0.6_{(3)}$	-	-	100.1	3	-	$1.99_{(1)}$	-	$0.01_{(1)}$	-	-	2.00
			Rds	-	-	$2.0_{(6)}$	$58.0_{(8)}$	-	$40_{(1)}$	100.0	3	-	-	$0.03_{(1)}$	$0.92_{(2)}$	-	$1.02_{(1)}$	1.98
			Ky	$36.2_{(1)}$	$63.8_{(4)}$	-	$0.6_{(2)}$	-	-	100.6	5	$0.97_{(2)}$	$2.02_{(2)}$	-	$0.02_{(1)}$	-	-	3.01
			Coe	$99.8_{(7)}$	-	-	$0.9_{(5)}$	-	-	100.7	2	$1.00_{(1)}$	-	-	$0.01_{(1)}$	-	-	1.00
1743-R	3.0	950	Sps	$36.1_{(6)}$	$21_{(1)}$	$1.4_{(2)}$	$41_{(1)}$	$0.5_{(2)}$	-	100.2	12	$2.96_{(6)}$	$2.1_{(1)}$	$0.09_{(1)}$	$2.84_{(9)}$	$0.04_{(2)}$	-	8.01
			Crn	-	$98.2_{(3)}$	-	$0.9_{(1)}$	-	-	99.1	3	-	$1.99_{(0)}$	-	$0.01_{(0)}$	-	-	2.00
			Ky	$36.5_{(1)}$	$62.7_{(1)}$	-	$1.4_{(1)}$	-	-	100.6	5	$0.99_{(0)}$	$1.99_{(0)}$	-	$0.04_{(0)}$	-	-	3.02
			Rds	-	-	$2.0_{(5)}$	$57.8_{(6)}$	$0.3_{(1)}$	$39.5_{(8)}$	100.0	3	-	-	$0.03_{(1)}$	$0.92_{(1)}$	-	$1.01_{(2)}$	1.98
			Coe	$99.4_{(2)}$	-	-	$0.9_{(1)}$	-	-	100.3	2	$1.00_{(0)}$	-	-	$0.01_{(0)}$	-	-	1.01
1215-R	3.0	1000	Sps	$36.4_{(2)}$	$20.6_{(1)}$	$1.6_{(2)}$	$41.3_{(6)}$	$0.5_{(1)}$	-	100.2	12	$2.99_{(2)}$	$1.99_{(1)}$	$0.11_{(2)}$	$2.88_{(3)}$	$0.04_{(1)}$	-	8.01
			Rds	-	-	$1.9_{(1)}$	$58_{(1)}$	$0.1_{(3)}$	$40_{(1)}$	100.0	3	-	-	$0.03_{(0)}$	$0.93_{(4)}$	-	$1.02_{(1)}$	1.98
			Crn	-	$99.8_{(1)}$	-	$0.4_{(1)}$	-	-	100.1	3	-	$2.00_{(0)}$	-	$0.00_{(1)}$	-	-	2.00
			Ky	$36.4_{(9)}$	$62.5_{(4)}$	-	$1.1_{(5)}$	-	-	100.0	5	$0.99_{(0)}$	$1.99_{(0)}$	-	$0.04_{(0)}$	-	-	3.02
			Coe	$99.7_{(1)}$	-	-	$0.7_{(4)}$	-	-	100.4	2	$1.00_{(0)}$	-	-	$0.01_{(1)}$	-	-	1.01
2129-R	6.3	1050	Ky	$36.3_{(9)}$	$62.7_{(1)}$	-	$1.0_{(7)}$	-	-	100.0	5	$0.99_{(1)}$	$2.00_{(4)}$	-	$0.03_{(1)}$	-	-	3.02
			Rds	-	-	$1.7_{(5)}$	$58.8_{(6)}$	-	$39.2_{(4)}$	100.0	3	-	-	$0.03_{(1)}$	$0.94_{(1)}$	-	$1.01_{(1)}$	1.99
			Coe	$100.0_{(4)}$	-	-	-	-	-	100.5	2	$1.00_{(0)}$	-	-	-	-	-	1.00
2117-R	6.3	1100	Sps	$36.1_{(3)}$	$20_{(1)}$	$1.3_{(1)}$	$41.9_{(4)}$	$0.5_{(3)}$	-	100.4	12	$3.01_{(5)}$	$1.92_{(8)}$	$0.09_{(1)}$	$2.96_{(5)}$	$0.05_{(3)}$	-	8.04
			Ky	$36.0_{(5)}$	$63.4_{(8)}$	-	$0.8_{(3)}$	-	-	100.2	5	$0.97_{(2)}$	$2.02_{(2)}$	-	$0.02_{(1)}$	-	-	3.01
			Crn	-	$100.0_{(7)}$	-	$0.4_{(1)}$	-	-	100.3	3	-	$2.00_{(0)}$	-	$0.01_{(1)}$	-	-	2.01
			Rds	-	$0.5_{(2)}$	$1.9_{(3)}$	$58.2_{(7)}$	-	$39.8_{(6)}$	100.0	3	-	-	$0.03_{(1)}$	$0.93_{(2)}$	-	$1.02_{(1)}$	1.98
			Coe	$99.8_{(4)}$	-	-	$0.8_{(3)}$	-	-	100.6	2	$1.00_{(0)}$	-	-	$0.01_{(1)}$	-	-	1.01
2143-R	7.5	1150	Ky	$36_{(1)}$	$63.7_{(2)}$	-	$0.7_{(1)}$	-	-	100.0	5	$0.96_{(3)}$	$2.04_{(4)}$	-	$0.02_{(1)}$	-	-	3.02
			Rds	-	-	$1.9_{(1)}$	$57.8_{(5)}$	-	$40.2_{(6)}$	100.0	3	-	-	$0.03_{(0)}$	$0.91_{(2)}$	-	$1.03_{(1)}$	1.98
			Coe	$99.9_{(6)}$	-	-	-	-	-	100.3	2	$1.00_{(0)}$	-	-	-	-	-	1.00
2144-R	7.5	1200	Sps	$36.6_{(2)}$	$21_{(1)}$	$1.0_{(9)}$	$41.7_{(4)}$	$0.5_{(1)}$	-	100.8	12	$3.02_{(2)}$	$1.94_{(8)}$	$0.05_{(1)}$	$2.96_{(1)}$	$0.05_{(1)}$	-	8.04
			Ky	$36.1_{(1)}$	$63.2_{(3)}$	-	$0.8_{(3)}$	-	-	100.1	5	$0.97_{(3)}$	$2.03_{(1)}$	-	$0.02_{(1)}$	-	-	3.02
			Rds	-	-	$2.0_{(1)}$	$58.1_{(3)}$	-	$39.9_{(5)}$	100.0	3	-	-	$0.03_{(0)}$	$0.91_{(1)}$	-	$1.03_{(1)}$	1.98
			Coe	$99.9_{(3)}$	-	-	-	-	-	99.9	2	$1.00_{(0)}$	-	-	-	-	-	1.00

Sps—spessartine, Coe—coesite, Crn—corundum, Ky—kyanite, Rds—rhodochrosite; *—calculated after the sum deficit; the values in parentheses are one sigma errors of the means based on replicate electron microprobe analyses reported as least units cited; $36.1_{(1)}$ should be read as 36.1 ± 0.1 wt.%.

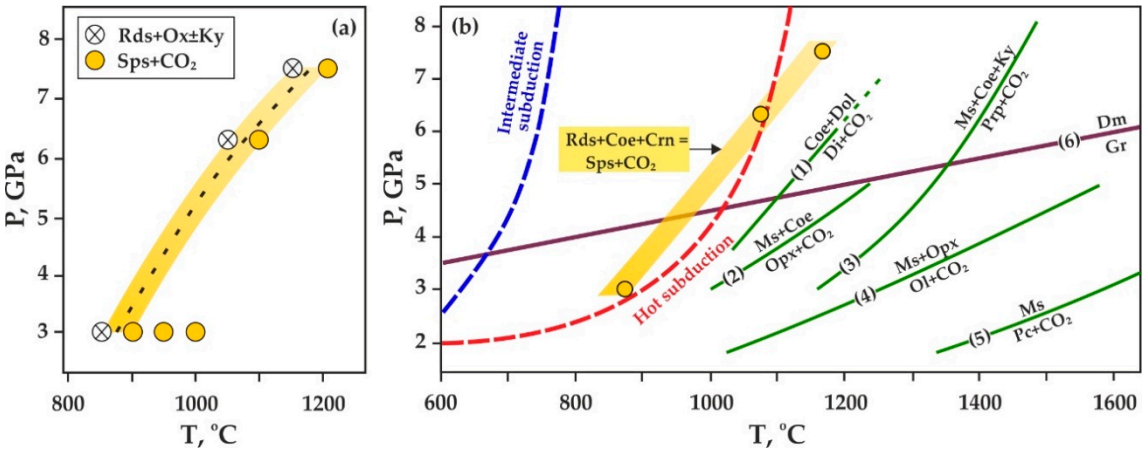

Figure 5. *P-T* diagrams with (**a**) experimentally determined decarbonation reaction, associated with the formation of spessartine and CO_2-fluid; and (**b**) previously constrained decarbonation curves after [39] (1), [40,41] (2), [23] (3), [42,43] (4), [44] (5) and graphite-diamond transition line (6) [45]. Ms—magnesite, Pc—periclase, Opx—enstatite, Ol—forsterite, Coe—coesite, Ky—kyanite, Prp—pyrope, Dm—diamond, Gr—graphite, Rds—rhodochrosite, Crn—corundum, Sps—spessartine, Ox—oxides.

These data indicate the effective operation of the hematite buffer and adequate experimental results. The obtained crystals of spessartine and recrystallized rhodochrosite were studied by Raman spectroscopy, and a comparative study of the characteristics of the synthesized garnets with the available literature data was carried out (Figure 4a–c, Table 3).

Table 3. Raman characterization of spessartine garnet, synthesized in $MnCO_3$-SiO_2-Al_2O_3 system and previously published data.

Run N	**1744-R**	**2117-R**	**Sps[1]**	**Sps[2]**	**Sps[2]$_{cal}$**
***P*, GPa**	**3.0**	**6.3**			
***T*, °C**	**950**	**1100**			
		Raman Shift, cm^{-1}			
	106	-	-	-	105
	163	164	162	162	163
	174	174	175	175	-
	-	195	196	196	195
	221	221	221	221	221
	270	-	269	269	-
	300	300	302	302	298
	-	-	-	-	314
	325	321	321	321	320
$R(SiO_4)^{4-}$	349	-	-	-	347
$R(SiO_4)^{4-}$	-	350	350	350	365
	376	371	372	372	375
	404	403	-	-	-
	415	-	-	-	-
	437	468	-	-	-
	-	473	475	475	475
	486	487	-	-	-
	-	500	500	500	505
	522	-	522	522	530
$(Si\text{-}O)_{bend}$, υ_2	553	553	552	552	560
	-	-	573	573	-
	-	-	592	592	587
	-	-	630	630	639
	-	848	849	849	845
	852	-	-	-	852
	-	-	879	879	876
$(Si\text{-}O)_{str}$, υ_1	907	906	905	905	910
$(Si\text{-}O)_{str}$, υ_1	-	-	913	913	913
	954	-	-	-	-
	-	1031	1029	1029	1033

[1]—According to [46]; [2]—according to [47]; Sps—spessartine.

The main characteristics of the Raman spectra of natural spessartine were modes near 350, 552, and 905 cm^{-1}, which were related to librational ($R(SiO_4)^{4-}$), internal bending ($(Si\text{-}O)_{bend}$, υ_2), and stretching ((Si-O)str, υ_1) vibrations of the SiO_4 tetrahedron, respectively [39]. In the Raman spectra of spessartine obtained as a result of decarbonation reactions, the main modes were 349–350, 552, and 906–907 cm^{-1} (Figure 4, Table 3). Peaks of 403–404, 415, 437, 468, 486, and 954 cm^{-1} were noted as secondary modes characteristic of spessartine resulting from decarbonation reactions and not found in the Raman spectra of natural Mn-rich garnet. In addition, in the Raman spectra of the obtained garnet, there were no peaks at 573, 592, 630, 879, or 913 cm^{-1}, characteristic of natural spessartine [39]. These differences can be explained by two possible reasons: (1) grossular and almandine components (even minor) can affect the Raman spectra of spessartine and (2) synthesized spessartine can contain micro inclusions of carbonate, kyanite, corundum, or coesite, which also reflects in Raman spectra.

4. Discussion

4.1. Conditions of Rhodochrosite-Involving Decarbonation Reactions and Comparison to the Stability of Other Carbonates

Most existing thermal and thermodynamic models [48–51] predict that decarbonation involving Mg and Ca carbonates is rarely realized along most subduction *P-T* paths (Figure 5b). These models predict that most subducted carbon will be transported to great depths. Modern theoretical and experimental works on the simulation of decarbonation reactions under mantle pressures and temperatures [39–44] and findings of carbonate inclusions in diamonds [52–60] confirm these ideas. However, there is a lack of studies devoted to the simulation of decarbonation reactions involving other carbonates than magnesite, calcite, and dolomite. As it is shown in Figure 4b, decarbonation of Ca,Mg-carbonate + oxide or Ca,Mg-carbonate + silicate assemblages occurs at temperatures much higher than it is intended for hot subduction. As it was demonstrated in the present study, Mn-carbonate is the most probable candidate to undergo decarbonation under hot subduction *P-T* paths. We have to emphasize that siderite is also a potential carbonate to be involved in decarbonation immediately in the undergoing slab, since Fe and Mn have many common basic chemical characteristics (both 3*d* transition metals that can have various valence and similar spin states). In this study, we determined the position of the decarbonation curve, resulting in the formation of nearly pure spessartine and CO_2 fluid. The spessartine crystallization and the CO_2-fluid liberation at a depth of ~90 km would occur at T of 800–900 °C and at a depth of ~190–225 km at 1070–1170 °C. However, taking into account that rhodochrosite is not widely distributed in the Earth's crust (compared to other carbonates), it is unlikely that pure spessartine would be widely distributed in the slab. More likely, carbonates in the subducting slab would form various solid solutions. For example, formation of $(Mn,Fe)CO_3$ and its further decarbonation most probably would result in spessartine-almandine garnet crystallization, whereas subduction of carbonate solid solutions of $(Mg,Mn)CO_3$ and $(Ca,Mn)CO_3$ compositions would potentially result in the partial decarbonation with the crystallization of Mn-rich garnet and preservation of Mg or Ca carbonate end-members in the down-going slab. One of the main implications of our research is the fact that the presence of $MnCO_3$ in subduction slab, even as solid solution with Mg,Ca-carbonates, would result in a decrease of the decarbonation temperatures. However, when reconstructing the possible mechanisms of the formation of Mn-rich garnet in terms of decarbonation reactions, one can notice that these reactions in nature can not only occur during slab subduction but also in other processes, such as kimberlite eruption [61,62].

4.2. Spessartine + CO_2 Formation and Possible Implications for Diamond or Graphite Genesis

In the Earth's mantle, Mn predominantly enters silicates, oxides, carbonates, and sulfides. Concentrations of MnO in mantle silicates are relatively low and amount, on average, to 0.05–0.35 wt.% in olivine [63], 0.06–0.20 wt.% in pyroxenes [64], and 0.2–0.4 wt.% in garnets [59,65,66]. Detailed investigation of the Mn content in these minerals was performed for geothermometry [64,65], and as a result, a wealth of data is available that let one notice mantle silicates with increased Mn concentrations.

The most interesting problem to discuss in these terms is a possible genesis of unusually Fe- and Mn-enriched garnets in assemblage with diamonds in several large localities worldwide: (1) Finsch kimberlite pipe, (2) West Greenland and Western Alps UHP terranes, and (3) Dachine, French Guiana. Diamonds of eclogitic paragenesis at Finsch kimberlitic pipe contain Fe- and Mn-enriched garnets as inclusions [13–17]. These garnets contain 15–27 wt.% FeO and up to 1.6 wt.% MnO [13]; they also demonstrate a positive correlation between MnO contents and Sr isotopic compositions. Isotopic characteristics showed that the carbon source for these diamonds was a protolith consisting of subducted oceanic crust enriched in Mn and Fe [16]. Formation conditions of these garnet inclusions are estimated to be 150–200 km and 900–1200 °C [13]. Diamond-bearing ultra-high pressure rocks from West Greenland and Western Alps demonstrate protoliths characterized by higher Fe and Mn contents that resulted from ocean-floor hydrothermal alteration compared to protoliths of both continental

and oceanic affinity from other UHP terranes [18–20]. Diamonds in these rocks occurred within spessartine-rich garnet as inclusions in syngenetic association with C–O–H fluid inclusions, SiO_2, and magnesite [18]. Diamonds from Dachine, French Guiana have unique eclogitic inclusions of Mn-rich garnet with MnO content of 12.8–18.8 wt.% [17]. The carbon source for these diamonds was established to be of crustal (seafloor) origin. All studies described above imply the participation of ocean crust materials as a source for both Mn-rich garnet formation and diamond crystallization. These sources, on the one hand, can be oceanic Mn-rich nodules and organic carbon and, on the other hand, Mn-carbonates, e.g., rhodochrosite. The data obtained in the present study demonstrate that rhodochrosite-involving decarbonation reactions can be a viable source for the spessartine component in diamond-assembling garnets and CO_2 fluid, acting as a carbon source for diamond crystallization.

5. Conclusions

- Our HP-HT experiments with a specially designed hematite-buffered high-pressure cell showed that decarbonation in the $MnCO_3$-SiO_2-Al_2O_3 system resulted in the formation of a CO_2-fluid and spessartine at 870 ± 20 °C (3.0 GPa), 1070 ± 20 °C (6.3 GPa), and 1170 ± 20 °C (7.5 GPa) along a hot subduction *P-T* path.
- Using the mass spectrometry method (IRMS), the effectiveness of the hematite buffer was demonstrated, and it was shown that the composition of the fluid, liberated as a result of decarbonation, corresponded to pure CO_2.
- An experimental reconstruction of the position of the decarbonation curve leading to the formation of a CO_2-fluid in assemblage with spessartine was carried out in *P-T* space. It was found that the experimentally determined decarbonation curve for the formation of spessartine + CO_2 was located 300–350 °C lower than that for pyrope + CO_2. Our results indicate that the formation of spessartine + CO_2 from the decarbonation of rhodochrosite under hot subduction settings would occur at a depth of ~90 km and 850–900 °C and at 190–225 km depth and 1070–1170 °C.
- We experimentally demonstrated that (1) the presence of rhodochrosite as solid solution with Mg,Ca-carbonates in the subducting slab can result in a significant decrease of the decarbonation temperatures, and (2) rhodochrosite decarbonation is an important reaction to explain the relationship between Mn-rich garnets and diamonds with subduction/crustal isotopic signature.

Author Contributions: Conceptualization, Y.V.B. and Y.N.P.; Data curation, Y.V.B. and Y.N.P.; Formal analysis, Y.V.B. and I.D.N.; Funding acquisition, Y.V.B.; Investigation, Y.V.B., A.N.K., and I.D.N.; Methodology, A.N.K. and Y.N.P.; Project administration, Y.V.B.; Visualization, Y.V.B. and I.D.N.; Writing—Original draft, Y.V.B.; Writing—Review & editing, Y.N.P. All authors have read and agreed to the published version of the manuscript.

Funding: This research was funded by Russian Foundation for Basic Research, grant number 18-35-20016, and by state assignment of IGM SB RAS.

Acknowledgments: The authors express their sincere thanks to Vadim N. Reutsky for the help in implementation of mass spectrometry analyses and to Yuri M. Borzdov and Alexander G. Sokol for scientific consultation.

Conflicts of Interest: The authors declare no conflict of interest. The funders had no role in the design of the study; in the collection, analyses, or interpretation of data; in the writing of the manuscript, or in the decision to publish the results.

References

1. Lyubetskaya, T.; Korenaga, J. Chemical composition of Earth's primitive mantle and its variance: 1. Method and results. *J. Geophys. Res. Space Phys.* **2007**, *112*, 1–21. [CrossRef]
2. McDonough, W.F. The Composition of the Earth. *Int. Geophys.* **1995**, *120*, 223–253. [CrossRef]
3. Wang, H.S.; Lineweaver, C.H.; Ireland, T.R. The elemental abundances (with uncertainties) of the most Earth-like planet. *Icarus* **2018**, *299*, 460–474. [CrossRef]
4. Allègre, C.J.; Manhes, G.; Lewin, É. Chemical composition of the Earth and the volatility control on planetary genetics. *Earth Planet. Sci. Lett.* **2001**, *185*, 49–69. [CrossRef]

5. Margolis, S.V.; Burns, R.G. Pacific Deep-Sea Manganese Nodules: Their Distribution, Composition, and Origin. *Annu. Rev. Earth Planet. Sci.* **1976**, *4*, 229–263. [CrossRef]
6. Santillán, J.; Williams, Q. A high-pressure infrared and X ray study of FeCO3 and $MnCO_3$: Comparison with CaMg (CO3)2-dolomite. *Phys. Earth Planet. Inter.* **2004**, *143–144*, 291–304.
7. Liu, L.-G.; Lin, C.-C.; Yang, Y.-J. Formation of diamond by decarbonation of $MnCO_3$. *Solid State Commun.* **2001**, *118*, 195–198. [CrossRef]
8. Ono, S. High-pressure phase transformation in $MnCO_3$: A synchrotron XRD study. *Miner. Mag.* **2007**, *71*, 105–111. [CrossRef]
9. Farfan, G.A.; Boulard, E.; Wang, S.; Mao, W.L. Bonding and electronic changes in rhodochrosite at high pressure. *Am. Miner.* **2013**, *98*, 1817–1823. [CrossRef]
10. Merlini, M.; Hanfland, M.; Gemmi, M. The $MnCO_3$-II high-pressure polymorph of rhodocrosite. *Am. Miner.* **2015**, *100*, 2625–2629. [CrossRef]
11. Boulard, E.; Goncharov, A.F.; Blanchard, M.O.; Mao, W.L. Pressure-induced phase transition in $MnCO_3$ and its implications on the deep carbon cycle. *J. Geophys. Res. Solid Earth* **2015**, *120*, 4069–4079. [CrossRef]
12. Boulard, E.; Liu, Y.; Koh, A.L.; Reagan, M.M.; Stodolna, J.; Morard, G.; Mezouar, M.; Mao, W.L. Transformations and Decomposition of $MnCO_3$ at Earth's Lower Mantle Conditions. *Front. Earth Sci.* **2016**, *4*, 107. [CrossRef]
13. Appleyard, C.; Viljoen, K.; Dobbe, R. A study of eclogitic diamonds and their inclusions from the Finsch kimberlite pipe, South Africa. *Lithos* **2004**, *77*, 317–332. [CrossRef]
14. Deines, P.; Gurney, J.; Harris, J. Associated chemical and carbon isotopic composition variations in diamonds from Finsch and Premier kimberlite, South Africa. *Geochim. Cosmochim. Acta* **1984**, *48*, 325–342. [CrossRef]
15. Deines, P. The carbon isotope geochemistry of mantle xenoliths. *Earth-Sci. Rev.* **2002**, *58*, 247–278. [CrossRef]
16. Smith, C.; Gurney, J.; Harris, J.; Otter, M.; Kirkley, M.; Jagoutz, E. Neodymium and strontium isotope systematics of eclogite and websterite paragenesis inclusions from single diamonds, Finsch and Kimberley Pool, RSA. *Geochim. Cosmochim. Acta* **1991**, *55*, 2579–2590. [CrossRef]
17. Smith, C.B.; Walter, M.J.; Bulanova, G.P.; Mikhail, S.; Burnham, A.D.; Gobbo, L.; Kohn, S.C. Diamonds from Dachine, French Guiana: A unique record of early Proterozoic subduction. *Lithos* **2016**, *265*, 82–95. [CrossRef]
18. Frezzotti, M.L.; Selverstone, J.; Sharp, Z.D.; Compagnoni, R. Carbonate dissolution during subduction revealed by diamond-bearing rocks from the Alps. *Nat. Geosci.* **2011**, *4*, 703–706. [CrossRef]
19. Groppo, C.; Beltrando, M.; Compagnoni, R. P-T path of the UHP Lago di Cignana and adjoining HP meta-ophiolitic units: Insights into the evolution of subducting Tethyan slab. *J. Metamorph. Geol.* **2009**, *27*, 207–231. [CrossRef]
20. Glassley, W.E.; Korstgård, J.A.; Sørensen, K.; Platou, S.W. A new UHP metamorphic complex in the ~1.8 Ga Nagssugtoqidian Orogen of West Greenland. *Am. Miner.* **2014**, *99*, 1315–1334. [CrossRef]
21. Sobolev, N.V.; Shatsky, V.S. Diamond inclusions in garnets from metamorphic rocks: A new environment for diamond formation. *Nature* **1990**, *343*, 742–746. [CrossRef]
22. Kaminsky, F.; Belousova, E. Manganoan ilmenite as kimberlite/diamond indicator mineral. *Russ. Geol. Geophys.* **2009**, *50*, 1212–1220. [CrossRef]
23. Knoche, R.; Sweeney, R.J.; Luth, R. Carbonation and decarbonation of eclogites: The role of garnet. *Contrib. Miner. Pet.* **1999**, *135*, 332–339. [CrossRef]
24. Palyanov, Y.N.; Sokol, A.G.; Tomilenko, A.A.; Sobolev, N.V. Conditions of diamond formation through carbonate-silicate interaction. *Eur. J. Miner.* **2005**, *17*, 207–214. [CrossRef]
25. Bataleva, Y.V.; Novoselov, I.D.; Kruk, A.N.; Furman, O.V.; Reutsky, V.N.; Palyanov, Y.N. Experimental modeling of decarbonation reactions resulting in the formation of Mg, Fe-garnets and CO_2-fluid under mantle P,T-parameters. *Russ. Geol. Geophys.* **2020**, *61*, 650–662.
26. Ogasawara, Y.; Liou, J.G.; Zhang, R.Y. Thermochemical calculation of logfO2-T-P stability relations of diamond-bearing assemblages in the model system CaO-MgO-SiO_2-CO_2-H_2O. *Russ. Geol. Geophys.* **1997**, *38*, 546–557.
27. Berman, R.G. Thermobarometry using multiequilibrium calculations: A new technique with petrologic applications. *Can. Mineral.* **1991**, *29*, 833–855.
28. Ovsyannikov, S.V.; Abakumov, A.M.; Tsirlin, A.A.; Schnelle, W.; Egoavil, R.; Verbeeck, J.; Van Tendeloo, G.; Glazyrin, K.V.; Hanfland, M.; Dubrovinsky, L. Perovskite-like Mn2O3. A path to new manganites. *Angew. Chem. Int. Ed. Eng.* **2013**, *52*, 1494–1498. [CrossRef]

29. Palyanov, Y.N.; Borzdov, Y.M.; Khokhryakov, A.F.; Kupriyanov, I.N.; Sokol, A.G. Effect of Nitrogen Impurity on Diamond Crystal Growth Processes. *Cryst. Growth Des.* **2010**, *10*, 3169–3175. [CrossRef]
30. Palyanov, Y.N.; Kupriyanov, I.N.; Khokhryakov, A.F.; Borzdov, Y.M. High-pressure crystallization and properties of diamond from magnesium-based catalysts. *CrystEngComm* **2017**, *19*, 4459–4475. [CrossRef]
31. Pal'Yanov, Y.N.; Sokol, A.G. The effect of composition of mantle fluids/melts on diamond formation processes. *Lithos* **2009**, *112*, 690–700. [CrossRef]
32. Sokol, A.; Borzdov, Y.M.; Palyanov, Y.N.; Khokhryakov, A.F. High-temperature calibration of a multi-anvil high pressure apparatus. *High Press. Res.* **2015**, *35*, 139–147. [CrossRef]
33. Sokol, A.; Khokhryakov, A.F.; Palyanov, Y.N. Composition of primary kimberlite magma: Constraints from melting and diamond dissolution experiments. *Contrib. Miner. Pet.* **2015**, *170*, 26. [CrossRef]
34. Santamaria-Perez, D.; McGuire, C.; Makhluf, A.; Kavner, A.; Chuliá-Jordán, R.; Pellicer-Porres, J.; García, D.M.; Doran, A.; Kunz, M.; Rodriguez-Hernandez, P.; et al. Exploring the Chemical Reactivity between Carbon Dioxide and Three Transition Metals (Au, Pt, and Re) at High-Pressure, High-Temperature Conditions. *Inorg. Chem.* **2016**, *55*, 10793–10799. [CrossRef]
35. Luth, R.W. Natural versus experimental control of oxidation state: Effects on the composition and speciation of C-O-H fluids. *Am. Mineral.* **1989**, *74*, 50–57.
36. Boettcher, A.L.; Mysen, B.O.; Allen, J.C. Techniques for the control of water fugacity and oxygen fugacity for experimentation in solid-media high-pressure apparatus. *J. Geophys. Res.* **1973**, *78*, 5898–5901. [CrossRef]
37. Reutsky, V.; Borzdov, Y.M.; Palyanov, Y.N. Carbon isotope fractionation associated with HPHT crystallization of diamond. *Diam. Relat. Mater.* **2008**, *17*, 1986–1989. [CrossRef]
38. Reutsky, V.; Borzdov, Y.; Palyanov, Y.; Sokol, A.; Izokh, O. Carbon isotope fractionation during experimental crystallisation of diamond from carbonate fluid at mantle conditions. *Contrib. Miner. Pet.* **2015**, *170*, 41. [CrossRef]
39. Luth, R.W. Experimental determination of the reaction dolomite + 2coesite = diopside + $2CO_2$ to 6GPa. *Contrib. Miner. Pet.* **1995**, *122*, 152–158. [CrossRef]
40. Wyllie, P.; Huang, W.-L.; Otto, J.; Byrnes, A. Carbonation of peridotites and decarbonation of siliceous dolomites represented in the system CaO-MgO-SiO_2-CO_2 to 30 kbar. *Tectonophys.* **1983**, *100*, 359–388. [CrossRef]
41. Eggler, D.H. The effect of CO_2 upon partial melting of peridotite in the system Na_2O-CaO-Al_2O_3-MgO-SiO_2-CO_2 to 35 kbar, with an analysis of melting in a peridotite-H_2O-CO_2 system. *Am. J. Sci.* **1978**, *278*, 305–343. [CrossRef]
42. Newton, R.; Sharp, W. Stability of forsterite + CO_2 and its bearing on the role of CO_2 in the mantle. *Earth Planet. Sci. Lett.* **1975**, *26*, 239–244. [CrossRef]
43. Koziol, A.M.; Newton, R.C. Experimental determination of the reaction; magnesite + enstatite = forsterite + CO_2 in the ranges 6–25 kbar and 700–1100°. *Am. Miner.* **1998**, *83*, 213–219. [CrossRef]
44. Shatskiy, A.; Litasov, K.D.; Palyanov, Y. Phase relations in carbonate systems at pressures and temperatures of lithospheric mantle: Review of experimental data. *Russ. Geol. Geophys.* **2015**, *56*, 113–142. [CrossRef]
45. Kennedy, C.S.; Kennedy, G.C. The equilibrium boundary between graphite and diamond. *J. Geophys. Res.* **1976**, *81*, 2467–2470. [CrossRef]
46. Kolesov, B.A.; Geiger, C.A. Raman spectra of silicate garnets. *Phys. Chem. Miner.* **1998**, *25*, 142–151. [CrossRef]
47. Valenzano, L.; Meyer, A.; Demichelis, R.; Civalleri, B.; Dovesi, R. Quantum-mechanical ab initio simulation of the Raman and IR spectra of $Mn_3Al_2Si_3O_{12}$ spessartine. *Phys. Chem. Miner.* **2009**, *36*, 415–420. [CrossRef]
48. Connolly, J.A. Computation of phase equilibria by linear programming: A tool for geodynamic modeling and its application to subduction zone decarbonation. *Earth Planet. Sci. Lett.* **2005**, *236*, 524–541. [CrossRef]
49. Gorman, P.J.; Kerrick, D.M.; Connolly, J.A.D. Modeling open system metamorphic decarbonation of subducting slabs. *Geochem. Geophys. Geosystems* **2006**, *7*, 04007. [CrossRef]
50. Molina, J.F. Carbonate stability and fluid composition in subducted oceanic crust: An experimental study on H_2O–CO_2-bearing basalts. *Earth Planet. Sci. Lett.* **2000**, *176*, 295–310. [CrossRef]
51. Poli, S.; Franzolin, E.; Fumagalli, P.; Crottini, A. The transport of carbon and hydrogen in subducted oceanic crust: An experimental study to 5 GPa. *Earth Planet. Sci. Lett.* **2009**, *278*, 350–360. [CrossRef]
52. Bulanova, G. The formation of diamond. *J. Geochem. Explor.* **1995**, *53*, 1–23. [CrossRef]

53. Brenker, F.; Vollmer, C.; Vincze, L.; Vekemans, B.; Szymanski, A.; Janssens, K.; Szaloki, I.; Nasdala, L.; Joswig, W.; Kaminsky, F. Carbonates from the lower part of transition zone or even the lower mantle. *Earth Planet. Sci. Lett.* **2007**, *260*, 1–9. [CrossRef]
54. Izraeli, E.S.; Harris, J.W.; Navon, O. Brine inclusions in diamonds: A new upper mantle fluid. *Earth Planet. Sci. Lett.* **2001**, *187*, 323–332. [CrossRef]
55. Kaminsky, F.; Wirth, R.; Schreiber, A. Carbonatitic inclusions in deep mantle diamond from juina, Brazil: New minerals in the carbonate-halide association. *Can. Miner.* **2013**, *51*, 669–688. [CrossRef]
56. Wang, A.; Pasteris, J.D.; Meyer, H.O.; Dele-Duboi, M.L. Magnesite-bearing inclusion assemblage in natural diamond. *Earth Planet. Sci. Lett.* **1996**, *141*, 293–306. [CrossRef]
57. Navon, O.; Hutcheon, I.D.; Rossman, G.; Wasserburg, G.J. Mantle-derived fluids in diamond micro-inclusions. *Nature* **1988**, *335*, 784–789. [CrossRef]
58. Schrauder, M.; Navon, O. Hydrous and carbonatitic mantle fluids in fibrous diamonds from Jwaneng, Botswana. *Geochim. Cosmochim. Acta* **1994**, *58*, 761–771. [CrossRef]
59. Sobolev, N. Mineral inclusions in diamonds from the Sputnik kimberlite pipe, Yakutia. *Lithos* **1997**, *39*, 135–157. [CrossRef]
60. Stachel, T.; Harris, J.W.; Brey, G.P. Rare and unusual mineral inclusions in diamonds from Mwadui, Tanzania. *Contrib. Miner. Pet.* **1998**, *132*, 34–47. [CrossRef]
61. Abersteiner, A.; Kamenetsky, V.S.; Pearson, D.G.; Kamenetsky, M.; Goemann, K.; Courtney-Davies, L.; Rodemann, T. Monticellite in group-I kimberlites: Implications for evolution of parental melts and post-emplacement CO_2 degassing. *Chem. Geol.* **2018**, *478*, 76–88. [CrossRef]
62. Bussweiler, Y.; Stone, R.S.; Pearson, D.G.; Luth, R.W.; Stachel, T.; Kjarsgaard, B.A.; Menzies, A. The evolution of calcite-bearing kimberlites by melt-rock reaction: Evidence from polymineralic inclusions within clinopyroxene and garnet megacrysts from Lac de Gras kimberlites, Canada. *Contrib. Miner. Pet.* **2016**, *171*, 65. [CrossRef]
63. Giuliani, A. Insights into kimberlite petrogenesis and mantle metasomatism from a review of the compositional zoning of olivine in kimberlites worldwide. *Lithos* **2018**, 322–342. [CrossRef]
64. Delaney, J.S.; Smith, J.V.; Dawson, J.B.; Nixon, P.H. Manganese thermometer for mantle peridotites. *Contrib. Miner. Pet.* **1979**, *71*, 157–169. [CrossRef]
65. Creighton, S. A semi-empirical manganese-in-garnet single crystal thermometer. *Lithos* **2009**, *112*, 177–182. [CrossRef]
66. Schulze, D.J.; Harte, B.; Valley, J.W.; Channer, D.M. Evidence of subduction and crust–mantle mixing from a single diamond. *Lithos* **2004**, *77*, 349–358. [CrossRef]